Journal of Nuclear Materials 385 (2009) 545–551

Contents lists available at ScienceDirect

Journal of Nuclear Materials

journal homepage: www.elsevier.com/locate/jnucmat

A study of hot deformation behavior and microstructural characterization of Mo–TZM alloy

S. Majumdar [a,*], R. Kapoor [a], S. Raveendra [b], H. Sinha [c], I. Samajdar [b], P. Bhargava [b], J.K. Chakravartty [a], I.G. Sharma [a], A.K. Suri [a]

[a] Materials Group, Bhabha Atomic Research Centre, Mumbai 400 085, India
[b] Department of Metallurgical Engineering and Materials Science, Indian Institute of Technology Bombay, Powai, Mumbai 400 076, India
[c] Indian Institute of Technology, Kharagpur, India

ARTICLE INFO

Article history:
Received 18 September 2008
Accepted 17 December 2008

ABSTRACT

Hot compression testing of Mo–TZM (Mo–0.5Ti–0.1Zr–0.02C) alloy was carried out between 600 and 900 °C employing strain rates from 0.001 s^{-1} to 1 s^{-1}. Both the constant strain rate and strain rate change test results showed that Mo–TZM possesses low strain rate sensitivity in this temperature range. Activation energy calculated by using strain rate change data and plotting temperature compensated strain rate (Z) vs. shear modulus corrected flow stress (σ/G) was found to be 290 kJ/mol. Electron back scattered diffraction (EBSD) and transmission electron microscopic (TEM) results obtained from the rapidly cooled deformed specimens revealed the formation of subgrains. Flow stress–plastic strain results and misorientation angles between subgrains showed an anomalous behavior at 800 °C.

1. Introduction

For the new generation high temperature nuclear reactors, there is a demand for the materials capable of withstanding the aggressive environment with respect to stress, radiation, liquid metal corrosion, etc. at high temperatures. Molybdenum and niobium base alloys are being considered as the most promising materials [1] for such applications where conventional nickel or cobalt base superalloys cannot be used. Mo possesses high strength and creep resistance at high temperatures, high thermal conductivity, low coefficient of thermal expansion and excellent corrosion resistance against liquid metals [2–7]. Mo–TZM is a potent Mo base alloy containing 0.5–0.8%Ti, 0.08–0.1%Zr, and 0.016–0.02%C (wt%). Due to solid solution strengthening and precipitation strengthening by complex carbides of titanium and zirconium, Mo–TZM possesses higher strength and creep resistance than unalloyed molybdenum at high temperatures [8–10]. The presence of carbides in the microstructure also increases the recrystallization temperature of Mo [8]. A large number of studies have been reported on the irradiation behavior of the alloy under different neutron energy, fluence, and irradiation temperatures [11–21]. Mo–TZM alloy shows void swelling and irradiation embrittlement behavior at temperatures below 800 °C. However, irradiation at temperatures greater than 800 °C results in little change in mechanical properties due to annihilation of point defects produced by neutron irradiation [4,21]. Thermally activated vacancy diffusion mechanism operates at these high temperatures causing reduction in defects and hence embrittlement. Mo–TZM, thus appears to be a suitable structural material for the nuclear reactors operated in the temperature range of 800–1000 °C.

Due to higher melting temperature, powder metallurgical techniques are preferred to produce Mo–TZM alloy [22]. The ductile–brittle transition temperature of the alloy decreases with progressive hot working of the sintered bars in the temperature range of 800–1400 °C [23,24]. Low strain rate sensitivity and occurrence of dynamic strain aging at the temperatures lower than 450 °C has been reported earlier [25,26]. Fracture toughness values and crack initiation and propagation behavior by monotonic and cyclic loading below and above DBTT have been identified [27,28,6,29]. Morito studied the tensile behavior of heat treated electron beam welded Mo–TZM and reported that the carbides precipitate along the grain boundaries and strengthen it, hence, suppressing intergranular embrittlement [30,31].

In the present investigation, hot compression tests were carried out on Mo–TZM alloy in its application temperature range of 600–900 °C at four different strain rates between 10^{-3} and 1 s^{-1}. Strain rate change tests were also conducted to compare with the tests at constant strain rate. The effect of deformation conditions on evolution of microstructure was studied by electron back scattered diffraction (EBSD) technique. Constitutive behavior $\sigma = f(\dot{\epsilon}, T, \epsilon)$ for assessment of deformation limits and deformation mechanisms responsible for evolution of microstructure were studied.

* Corresponding author. Tel.: +91 22 25590183; fax: +91 22 25505151.
E-mail address: sanjib@barc.gov.in (S. Majumdar).

0022-3115/$ - see front matter © 2008 Elsevier B.V. All rights reserved.
doi:10.1016/j.jnucmat.2008.12.049

2. Experimental procedure

Mo–TZM alloy was prepared by arc melting the electrode made by pressing and sintering. Table 1 represents the detailed chemical composition of arc-consolidated alloy. Cylindrical specimens of 5 mm diameter and 7 mm height were prepared from the alloy plate. Since the microstructure of the as-received materials was heterogeneous with highly elongated grains, the specimens were annealed at 1650 °C for 2 h under reducing atmosphere. Hot compression tests were conducted at constant true strain rate under argon atmosphere. The samples were heated to four different temperatures ranging from 600 to 900 °C and deformed up to the maximum strain of 0.6 at four different true strain rates of 0.001, 0.01, 0.1 and 1 s^{-1}. Constant true strain rate $\dot{\epsilon}$ for a sample of initial height h_o was achieved by varying the ram velocity v with time t as $v = h_o\dot{\epsilon}\exp(-\dot{\epsilon}t)$. In addition to these tests, strain rate change tests were also conducted by deforming the specimens incrementally by changing strain rates in steps from 1 to 0.001 s^{-1} and subsequently from 0.001 to 1 s^{-1}. At the starting strain rate of 1 s^{-1} the samples were deformed to true strain of 0.25, after which at each subsequent strain rate of 0.1, 0.01, 0.001, 0.01, 0.1 and 1 s^{-1}, the samples were deformed in steps of 0.05 true strain. After each hot compression tests, the specimens were quenched in water. A thermocouple was placed on to the sample and the temperature was controlled within ±2 °C. At each temperature a new sample was deformed. The deformed specimens were sectioned along the compression axis and prepared for metallographic examination using standard techniques that involve polishing of samples using different grades of emery papers (60–600 ASTM sizes) up to 1 μm diamond finish. The specimens were further electropolished using a bath consisting of 88% (by volume) Methanol and 12% H_2SO_4, applying a potential of 20 V for 30 s at 15 °C. Electron back scattered diffraction (EBSD) studies of the electropolished samples were carried out in an orientation imaging microscope (FEI make). Electron beam scanning speed was maintained at 0.5 μm. Grain size, grain orientation spread (GOS) and grain average misorientation (GAM) were calculated from the EBSD data. Transmission electron microscopic (TEM) studies were also carried out to characterize subgrain structure. Thin slices were also cut along the compression axis and 3 mm diameter TEM samples were prepared by optimizing jet thinning parameters as 30 V and −50 °C using the electrolyte consisting of 20 vol.% perchloric acid and methanol solution.

Table 1
Chemical composition of arc cast Mo–TZM alloy.

Material	Elements (ppm in wt%)								
	C	O	N	Ti	Zr	Fe	Ni	Si	Mo
Mo–TZM	220	20	10	5000	1100	<10	<10	<10	Rest

3. Results and discussion

3.1. Stress–strain behavior

The true stress σ vs. plastic true strain ε for this TZM alloy at different strain rates and temperatures are shown in Fig. 1. From the

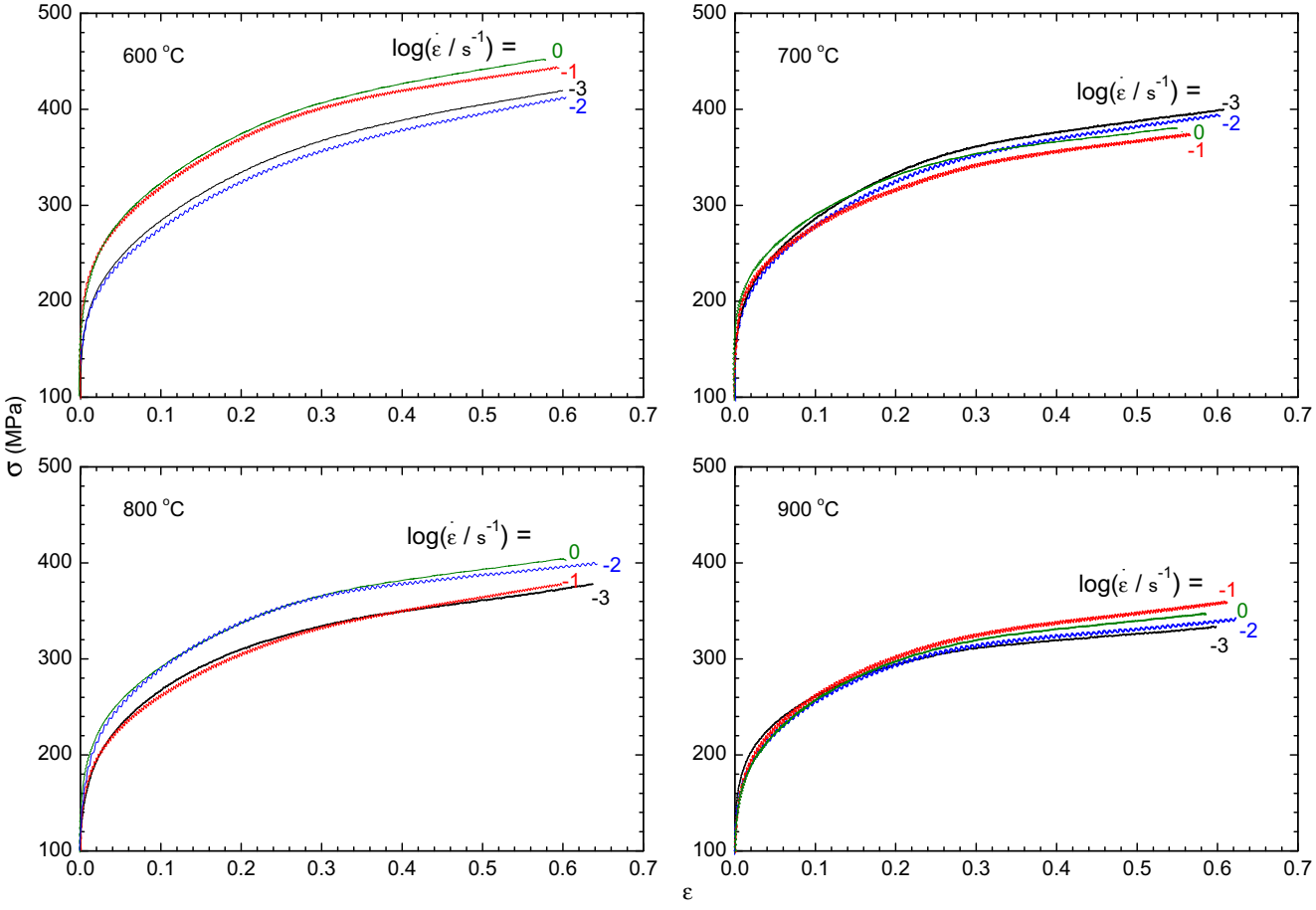

Fig. 1. True stress–true strain plots obtained from the compression tests conducted at 600, 700, 800 and 900 °C applying four strain rates 0.001, 0.01, 0.1 and 1 s^{-1}.

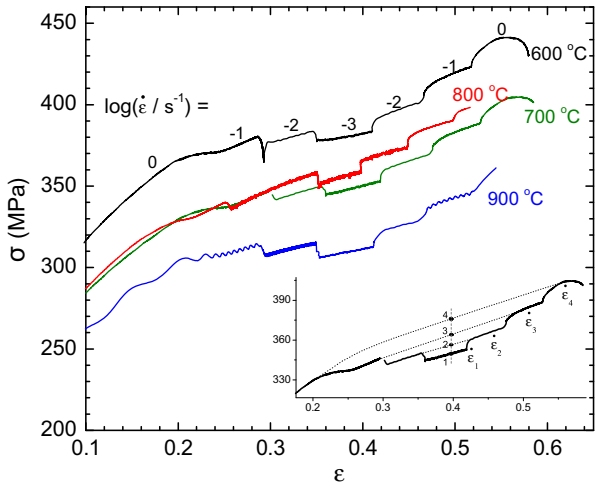

Fig. 2. Results of strain rate changed tests at different temperatures; inset shows an example of estimating the stress at the changed strain rates (at 700 °C).

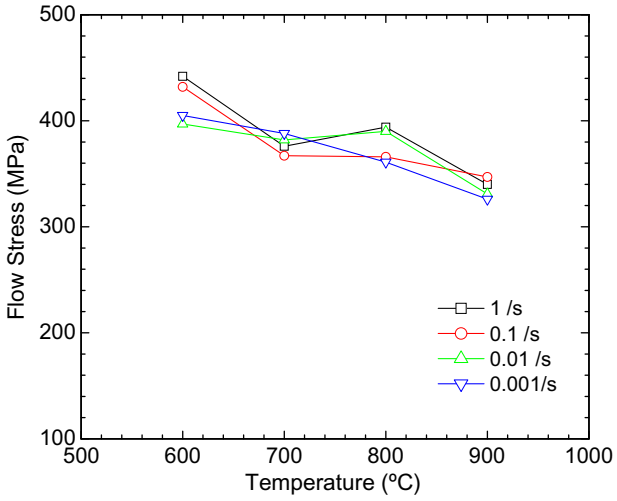

Fig. 4. Flow stress vs. temperature plots at different strain rates.

behavior of the constant strain rate (straight) tests it is seen that there is little apparent sensitivity of the flow stress to strain rate. At each of the temperatures the σ–ε curves are bunched together. Results obtained from strain rate change tests are shown in Fig. 2. With increasing temperature the flow stress reduces except at 800 °C. The flow stress values for each of the strain rates were estimated by interpolating the flow stress between the two segments of the same $\dot{\varepsilon}$ as shown in the inset of Fig. 2. For example, for $\dot{\varepsilon}_1$ the flow stress σ_1 was chosen at point '1', for $\dot{\varepsilon}_2$ the flow stress σ_2 was chosen at point '2' and so on. The $\sigma_i - \dot{\varepsilon}_1$ values obtained using this method are plotted along with the $\sigma - \dot{\varepsilon}$ values from straight tests (at $\varepsilon = 0.4$) as shown in Fig. 3. The $\sigma - \dot{\varepsilon}$ data for the straight tests also follow the trend of the strain rate change test. It is seen that the strain rate change test data at 800 °C lies slightly higher than that at 700 °C. This is similar to the trend observed in Fig. 2. Fig. 4 shows the flow stress at $\varepsilon = 0.5$ of the straight tests as a function of temperature. There is an overall trend of decreasing σ with increasing T, however for most strain rates σ at 800 °C appears higher than that at 700 °C. This apparent increase in flow stress observed between 700 °C and 800 °C might look like due to scatter in data. But the sample grain size is about 42 μm, whereas the diameter of sample is 5 mm, which shows that about 100 grains are present across the diameter of the sample, and will not result in data scatter. This temperature range of testing of Mo–TZM is in the athermal region of the material where both the temperature and strain rate sensitivity of stress are very low. It may be due to this the flow stress appears to have a scatter in the straight tests. Therefore strain rate change tests were carried out to obtain the strain rate sensitivity. Fig. 4 shows that the three tests at 800 °C (0.01, 0.1, 1 s^{-1}) all show similar trends compared to the 700 °C results: that the flow stress at 800 °C is equal to or higher than that at 700 °C except at the strain rate of 0.001 s^{-1}. Thus although there may be individual scatter, the overall trend does show a hardening at 800 °C.

The $\sigma - \dot{\varepsilon}$ data from the strain rate change tests as shown in Fig. 3 are re-plotted in Fig. 5 as temperature compensated strain rate or the Zener–Holloman parameter [32], $Z = \dot{\varepsilon}\exp(Q/RT)$ vs. σ/G, where Q is the activation energy and G is the shear modulus. Here shear modulus of pure Mo was taken as $G = 134(1 - 0.42(T - 300)/2883)$ [33] where T is in Kelvin. It is seen that the data for 600, 700 and 900 °C fall well onto a single line. The best fit for

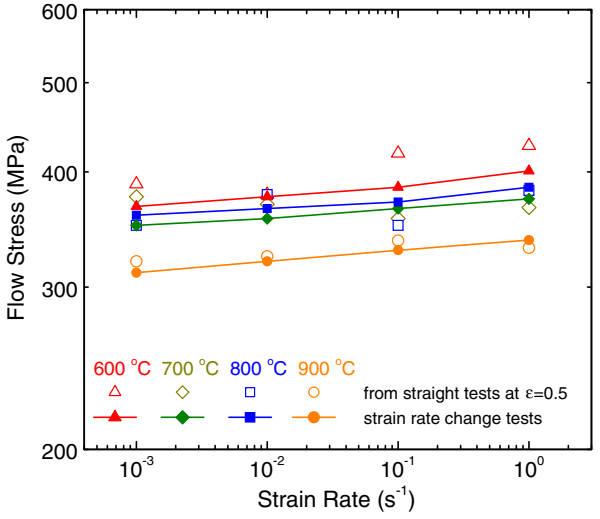

Fig. 3. Plots of flow stress vs. strain rate at different temperatures showing a very low strain rate sensitivity in this temperature range.

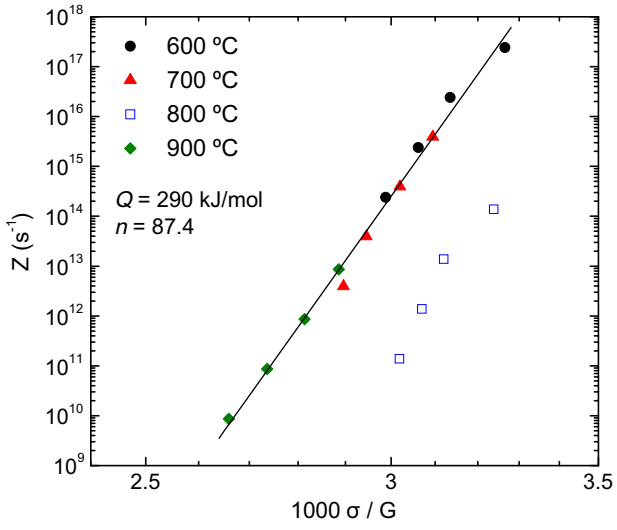

Fig. 5. Temperature compensated strain rate Z as function of stress normalized with shear modulus at different tested temperatures. The straight line is a fit to the 600, 700 and 900 °C data.

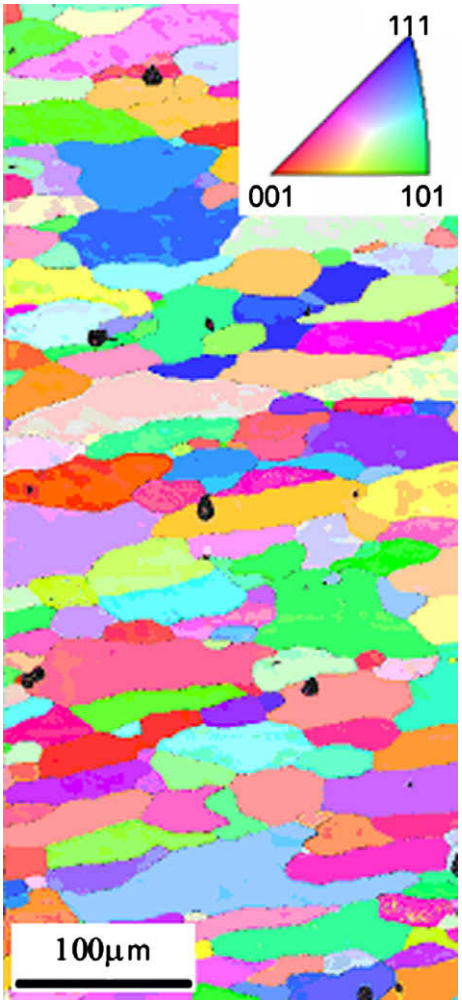

Fig. 6. EBSD microstructure of undeformed Mo–TZM alloy showing the formation of elongated grains grown along a preferred direction during annealing at 1650 °C for 2 h. The color codes in the inverse pole figure (inset) indicating the orientation of the grains at different crystallographic directions.

this is obtained for the values of Q = 290 kJ/mol and n = 87. This shows that the data fits a power-law of the type $Z = A(\sigma/G)^n$. The activation energy of self diffusion is reported to vary between 386 and 405 kJ/mol [34]. But the lower activation energy of 240 kJ/mol was also reported for creep of pure molybdenum in the temperature range of 1300–1600 °C [35]. A value of n = 87 is considered high and signifies a very low strain rate sensitivity $m = 1/n$ of 0.011. The manifestation of this low m was seen earlier in the bunching together of the flow curves at different strain rates (Fig. 1). The data at 800 °C was excluded from the fitting process as it could not be fit together with the same Q used for the 600, 700 and 900 °C data, but is shown here for comparison.

3.2. Microstructural characterization

EBSD microstructure of the annealed Mo–TZM specimen is presented in Fig. 6. The grains are mostly elongated in nature indicating a preferred directional grain growth during annealing at 1650 °C. The average grain size is found to be of the order of 42 μm. Grain boundary identification using either criteria of the misorientation angles 1° and 5° resulted in identical average grain size values. Fig. 7 represents the deformed microstructures at four hot compression tested temperatures at the strain rates 1 s^{-1}. The EBSD maps indicate that the deformation has mostly occurred by shear. Many shearing zones are present in the microstructures, especially for the samples deformed at higher strain rate of 1 s^{-1}(Fig. 7b and c). The formation of shear bands at high strain rates in other body centered cubic refractory metal alloys like Ta–W has been reported [36]. It was reported that at higher strain rates dynamic recovery occurs within a highly localized deformation region and the temperature rise associated with this deformed region is insufficient to achieve dynamic recrystallization. To accommodate the strain imposed on the material during deformation and to ensure compatibility with the surrounding grains, additional dislocations, geometrically necessary ones [37], result in substructures. During dynamic recovery, these dislocations tend to rearrange themselves into lower energy configuration by reducing lattice curvature (<5°) forming subgrains. The detailed analysis of all the EBSD maps of deformed specimens indicates that subgrains have formed during hot compression of Mo–TZM alloy as shown in the inset of Fig. 7(b). Small equiaxed grains, with very different orientations than neighboring grains observed at some places (Fig. 7), might have been formed due to localized recrystallization. Kang et al. [38] adopted a semi manual technique to distinguish between the subgrains separated by the misorientation angles >2.5°, >5° and >15°. In the present study, the calculations were performed using the misorientation angle >1°. Fig. 8 shows the change in average grain size with temperature and strain rate. The orientation spread between the grains is presented in Fig. 9. The average size and misorientation angle indicate that the deformed structure is mainly constituted of subgrains. Gillis et al. [39] reported that the relation between glide system reorientation strain forming tilt or twist boundaries is different for compression than it is in tension. Misorientation angle between the subgrains formed by compression should be lower than that in tension. It is clear from Fig. 8 that subgrain size is higher at higher strain rate and it decreases with increase in temperature from 600 to 800 °C. The apparent decrease in grain size detected in the EBSD patterns could be due to the flattening of the grains during the compression tests. Although the substructure does influence the flow stress behavior, a direct relation between subgrain size and flow stress cannot be established until steady state has been reached [40]. At steady state, the subgrains are uniform and equiaxed and size is inversely proportional to further increase in stress. From the stress–strain curves (Fig. 1) it is evident that the steady state is not reached. Therefore, it is difficult to explain the relationship between the subgrain size and strain rate. Fig. 10 shows the variation of grain average misorientation (GAM) with strain rate and temperature. GAM decreases with increase in temperature up to 800 °C. At 900 °C, all the three microstructural features, i.e. grain size, GOS and GAM are larger. This anomalous behavior may be due to the migration of solute particles to the boundaries restricting the recovery process. As the recovery process is hindered the misorientation angle between the subgrains is increased. Occurrence of dynamic strain aging (DSA) in molybdenum base system in the temperature range of 800–1400 °C has been reported [23] earlier. Thus it is likely that the anomalous behavior at 800 °C observed in the current study could be due to DSA operating at this temperature. A linear relationship has been reported between misorientation angle (θ) and subgrain size (d), and is given by $\theta = kd$, k is a constant [41]. The value of k calculated from our results is close to 0.3° μm^{-1} at all the temperatures except at 900 °C. The results obtained from our calculations using a misorientation angle >5 ° are presented in Table 2. The average grain size varied from 12 to 20 μm with a maximum misorientation of 5.68°. No particular trend in variation of grain size or GOS with temperature and strain rate is detected. The specimens tested at 600 °C were further characterized by transmission electron microscopy. Fig. 11(a) and (b) represents the bright field TEM image of the specimens deformed at 0.001 and 1 s^{-1}, respectively. In the specimen deformed at

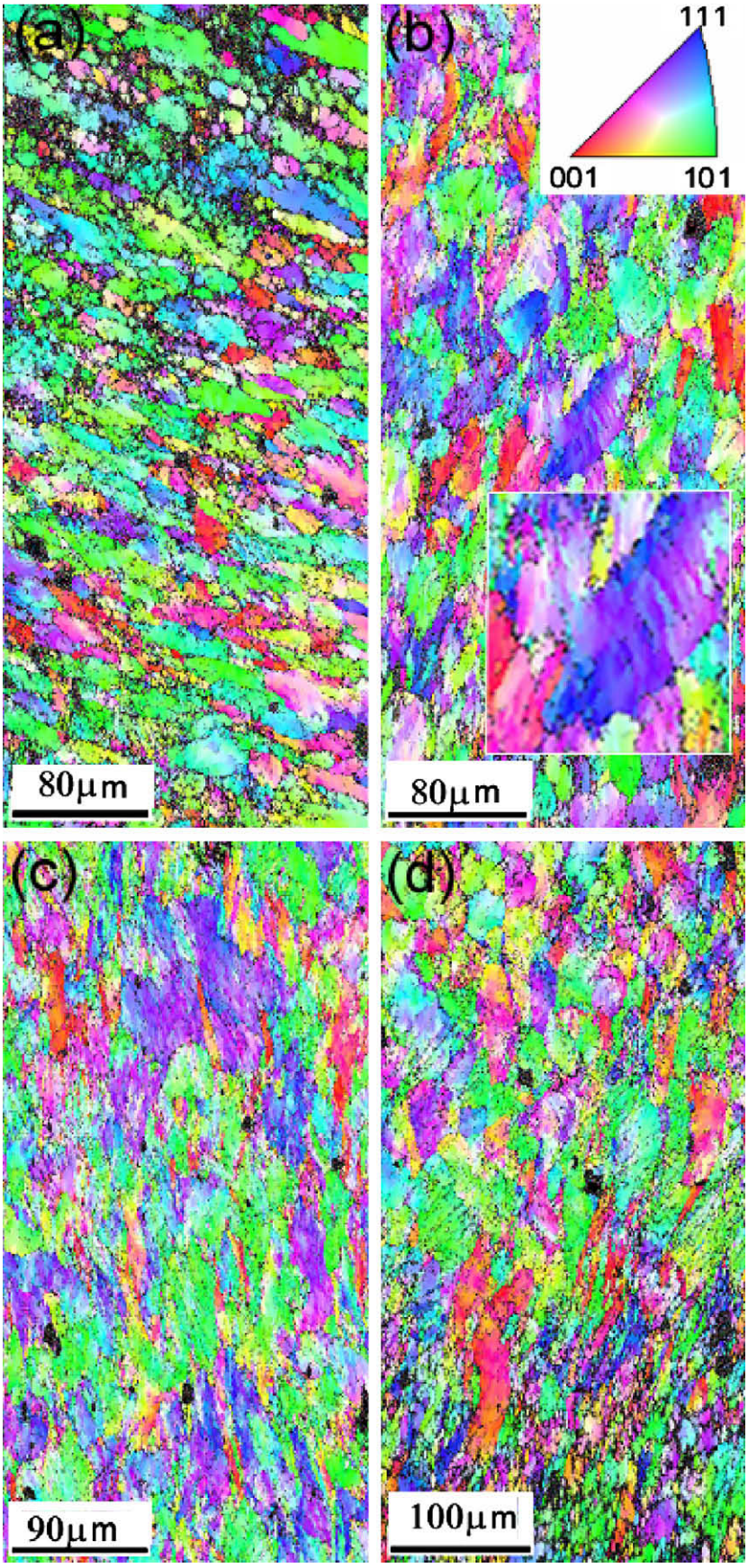

Fig. 7. EBSD images obtained from the specimens deformed at a strain rate of 1 s^{-1}; (a) 600 °C, (b) 700 °C, (c) 800 °C, and (d) 900 °C; inset in fig. b is a magnified view showing the subgrains.

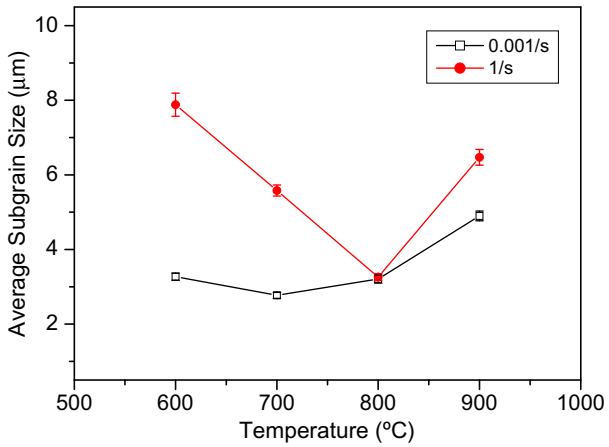

Fig. 8. Change in average subgrain size with temperature at the lowest and the highest strain rates studied. The minimum misorientation angle between the grains is used as 1° during calculation of grain size.

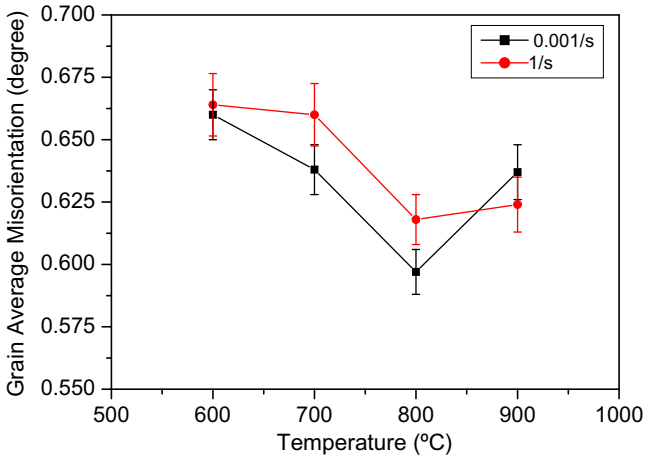

Fig. 10. Plots of grain average misorientation (GAM) against temperature showing the similar increasing trend as GOS from 800 to 900 °C for both the strain rates of 0.001 and 1 s^{-1}. Minimum misorientation angle used for calculation is 1°.

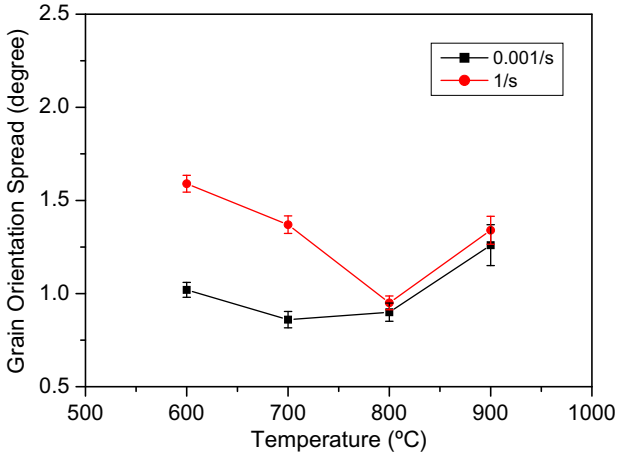

Fig. 9. Plots of grain orientation spread (GOS) against temperature showing an increase in GOS at 800 and 900 °C at strain rate of 0.001 s^{-1} and at 900 °C for 1 s^{-1}. Minimum misorientation angle used for calculation is 1°.

Table 2
Average grain size and grain orientation spread (GOS) of the specimens deformed at two different strain rates; misorientation angle >5°.

Temp (°C)	Grain size (μm)		GOS (°)	
	0.001 s^{-1}	1 s^{-1}	0.001 s^{-1}	1 s^{-1}
600	21.28 ± 1.92	16.73 ± 1.05	5.55 ± 0.2	4.26 ± 0.22
700	12.1 ± 0.81	23.08 ± 1.63	4.29 ± 0.24	5.68 ± 0.25
800	11.58 ± 0.67	20.05 ± 1.36	4.15 ± 0.27	5.08 ± 0.17
900	19.99 ± 1.24	15.35 ± 0.89	5.44 ± 0.56	4.58 ± 0.36

Grain size of the annealed material ~42 μm.

0.001 s^{-1}, the structures similar to that of cells are observed at the subgrain boundaries (Fig. 11(a)). Accumulation of a large number of dislocations along the boundary (Fig. 11(b)) is observed at the strain rate of 1 s^{-1}. The boundaries appear like dense dislocation walls [42]. It is evident from Fig. 11 that the subgrain size at 1 s^{-1} is larger compare to that formed at 0.001 s^{-1}. Similar results are also obtained from EBSD analysis.

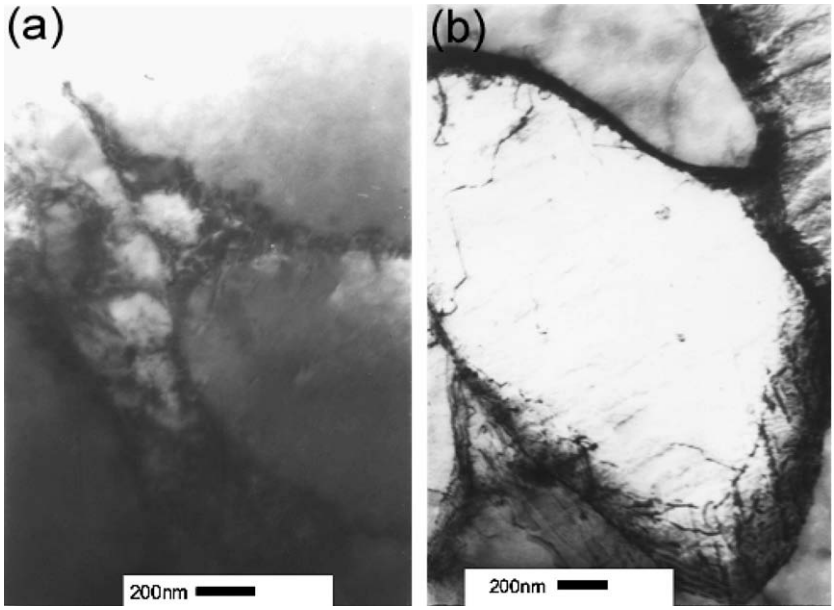

Fig. 11. TEM image showing subgrain structure with dislocation networks formed during hot compression at 600 °C for the strain rates (a) 0.001 s^{-1} and (b) 1 s^{-1}.

4. Conclusions

True stress–true plastic strain data were obtained from Mo–TZM alloy at the temperatures between 600 and 900 °C using hot compression testing. During continuous compression, bunching of the flow curves at different strain rates indicated lower strain rate sensitivity of the alloy in this temperature range. The temperature independent stress exponent (n) and the activation energy (Q) calculated using the data obtained from strain rate change tests in this temperature range were found to be 87 and 290 kJ/mol, respectively. Microstructural characterization revealed the formation of subgrains during hot deformation. An anomalous behavior of increase in flow stress and misorientation angle between the subgrains was observed at 800 °C.

Acknowledgements

Authors are thankful to Mr R. Fotedar for extending his facility for annealing of the alloy specimens. Authors wish to thank Mrs P. Agahse of Materials Science Division for her assistance in making TEM samples.

References

[1] M.S. El-Genk, J.M. Tournier, J. Nucl. Mater. 340 (2005) 93.
[2] B.V. Cockeram, Metall. Mater. Trans. A 36 (2005) 1777.
[3] A.P. Alur, N. Chollacoop, K.S. Kumar, Acta Mater. 52 (2004) 5571.
[4] B.V. Cockeram, R.W. Smith, L.L. Snead, J. Nucl. Mater. 346 (2005) 145.
[5] H.A. Calderon, G. Kostorz, G. Ullrich, Mater. Sci. Eng. A 160 (1993) 189.
[6] A.P. Alur, K.S. Kumar, Acta Mater. 54 (2006) 385.
[7] J.J. Park, D.P. Butt, C.A. Beard, Nucl. Eng. Des. 196 (2000) 315.
[8] T. Mrotzek, A. Hoffmann, U. Martin, Int. J. Refract. Met. Hard Mater. 24 (2006) 298.
[9] J. Warren, Int. J. Refract. Met. Hard Mater. 16 (1998) 149.
[10] N.E. Ryan, J.W. Martin, J. Less-Common Met. 17 (1969) 363.
[11] D.S. Gellas, D.T. Peterson, J.F. Bates, J. Nucl. Mater. 103&104 (1981) 1141.
[12] B.N. Singh, J.H. Evans, A. Horsewell, P. Toft, D.J. Edwards, J. Nucl. Mater. 223 (1995) 95.
[13] K. Abe, T. Masuyama, M. Satou, M.L. Hamilton, Mater. Trans., JIM 34 (1993) 1137.
[14] J.F. Stubbins, J. Moteff, J. Nucl. Mater. 103&104 (1981) 1163.
[15] T. Noda, M. Okada, R. Watanabe, J. Nucl. Mater. 91 (1980) 103.
[16] J.M. Steichen, J. Nucl. Mater. 60 (1976) 13.
[17] B.V. Cockeram, R.W. Smith, L.L. Snead, J. Nucl. Mater. 346 (2005) 165.
[18] Y. Aono, E. Kuramoto, N. Yoshida, Mater. Trans., JIM 34 (1993) 1130.
[19] B.N. Singh, A. Horsewell, P. Toft, J.H. Evans, J. Nucl. Mater. 212–215 (1994) 1292.
[20] K. Abe, M. Kikuchi, K. Tate, S. Morozumi, J. Nucl. Mater. 122&123 (1984) 671.
[21] T.S. Byun, M. Li, B.V. Cockeram, L.L. Snead, J. Nucl. Mater. 376 (2008) 240.
[22] D.R. Ervin, D.L. Bourell, C. Persad, L. Rabenberg, Mater. Sci. Eng. A 102 (1988) 25.
[23] R. Eck, E. Pink, Int. J. Refract. Met. Hard Mater. 11 (1992) 337.
[24] A.J. Mueller, J.A. Shields, R.W. Buckman, Metallwerk Plansee, Reutte, 1989, p. 37.
[25] G. Filacchioni, E. Casagrande, U. De Angelis, G. De Santis, D. Ferrara, J. Nucl. Mater. 307–311 (2002) 705.
[26] G. Filacchioni, E. Casagrande, U. De Angelis, G. De Santis, D. Ferrara, J. Nucl. Mater. 212–215 (1994) 1288.
[27] B.V. Cockeram, Mater. Sci. Eng. A 418 (2006) 120.
[28] M.F. Maday, J. Nucl. Mater. 233–237 (1996) 1397.
[29] B.V. Cockeram, Metall. Mater. Trans. A 33 (2002) 3685.
[30] F. Morito, J. Less-Common Met. 146 (1989) 337.
[31] F. Morito, J. Nucl. Mater. 212–215 (1994) 1608.
[32] C. Zener, J.H. Holloman, J. Appl. Phys. 15 (1944) 22.
[33] H.J. Frost, M.F. Ashby, Deformation Mechanism Maps, The Plasticity and Creep of Metals and Ceramics, Pergamon Press, Oxford, UK, 1982.
[34] J. Askill, D.H. Tomlin, Philos. Mag. 8 (1963) 997.
[35] J. Ciulik, E.M. Taleff, Mater. Sci. Eng. A 463 (2007) 197.
[36] M.T. Perez-prado, J.A. Hines, K.S. Vecchio, Acta Mater. 49 (2001) 2905.
[37] H. Weiland, Acta Metall. Mater. 40 (1992) 1083.
[38] J.Y. Kang, B. Bacroix, H. Regle, K.H. Oh, H.C. Lee, Acta Mater. 55 (2007) 4935.
[39] P.P. Gillis, E.G. Zukas, W.V. Green, Scripta Metall. 4 (1970) 855.
[40] J.J. Urcola, C.M. Sellars, Acta Metall. 35 (1987) 2649.
[41] H. Xiaoxu, K. Tsuzaki, T. Maki, Acta Metall. Mater. 43 (1995) 3375.
[42] Q. Liu, D.J. Jensen, N. Hansen, Acta Mater. 46 (1998) 5819.